



Defluorination of perfluorooctanoic acid and perfluorooctane sulfonic acid by heterogeneous catalytic system of Fe-Al₂O₃/O₃: Synergistic oxidation effects and defluorination mechanism

Yumin Zhang^a, Zhijie Guan^b, Xiaojian Liao^a, Yu Huang^a, Zhenhua Huang^a, Zhihua Mo^a, Baixuan Yin^a, Xingfan Zhou^a, Wencan Dai^a, Jialin Liang^d, Shuiyu Sun^{a,c,*}

^a Guangzhou Key Laboratory Environmental Catalysis and Pollution Control, Guangdong Key Laboratory of Environmental Catalysis and Health Risk Control, School of Environmental Science and Engineering, Institute of Environmental Health and Pollution Control, Guangdong University of Technology, Guangzhou 510006, China

^b Guangdong Eco-Engineering Polytechnic, Guangzhou 510520, China

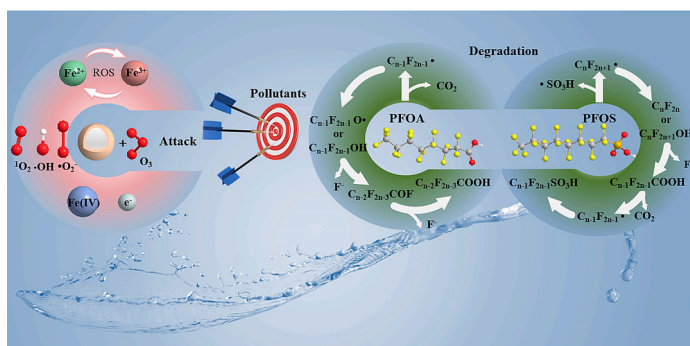
^c Guangdong Province Solid Waste Recycling and Heavy Metal Pollution Control Engineering Technology Research Center, Guangdong Polytechnic of Environmental Protection Engineering, Foshan 528216, China

^d Engineering and Technology Research Center for Agricultural Land Pollution Integrated Prevention and Control of Guangdong Higher Education Institute, College of Resources and Environment, Zhongkai University of Agriculture and Engineering, Guangzhou 510225, China

HIGHLIGHTS

- Fe-Al₂O₃ showed excellent catalytic performance.
- Using DFT calculations to find specific attack sites for PFOA and PFOS.
- The co-existence of ROS and Fe(IV) constituted a synergistic oxidation system.
- The degradation and defluorination pathways of PFOA and PFOS had been revealed.
- PFOS exhibited a higher DeF rate due to its susceptibility to electrophilic attack.

GRAPHICAL ABSTRACT



ARTICLE INFO

Editor: Jay Gan

Keywords:

Ozonation catalytic oxidation
Perfluorooctanoic acid
Perfluorooctane sulfonic acid
Synergistic oxidation effects
Defluorination

ABSTRACT

In this study, catalytic ozonation by Fe-Al₂O₃ was used to investigate the defluorination of PFOA and PFOS, assessing the effects of different experimental conditions on the defluorination efficiency of the system. The oxidation mechanism of the Fe-Al₂O₃/O₃ system and the specific degradation and defluorination mechanisms for PFOA and PFOS were determined. Results showed that compared to the single O₃ system, the defluorination rates of PFOA and PFOS increased by 2.32- and 5.92-fold using the Fe-Al₂O₃/O₃ system under optimal experimental conditions. Mechanistic analysis indicated that in Fe-Al₂O₃, the variable valence iron (Fe) and functional groups containing C and O served as important reaction sites during the catalytic process. The co-existence of ¹O₂, •OH,

* Corresponding author at: Guangzhou Key Laboratory Environmental Catalysis and Pollution Control, Guangdong Key Laboratory of Environmental Catalysis and Health Risk Control, School of Environmental Science and Engineering, Institute of Environmental Health and Pollution Control, Guangdong University of Technology, Guangzhou 510006, China.

E-mail address: sysun@gdut.edu.cn (S. Sun).

<https://doi.org/10.1016/j.scitotenv.2023.169675>

Received 8 October 2023; Received in revised form 23 December 2023; Accepted 23 December 2023

Available online 9 January 2024

0048-9697/© 2024 Elsevier B.V. All rights reserved.

$\cdot\text{O}_2^-$ and high-valence Fe(IV) constituted a synergistic oxidation system consisting of free radicals and non-radicals, promoting the degradation and defluorination of PFOA and PFOS. DFT theoretical calculations and the analysis of intermediate degradation products suggested that the degradation pathways of PFOA and PFOS involved Kolbe decarboxylation, desulfonation, alcoholization and intramolecular cyclization reactions. The degradation and defluorination pathways of PFOA and PFOS consisted of the stepwise removal of $-\text{CF}_2-$, with PFOS exhibiting a higher defluorination rate than PFOA due to its susceptibility to electrophilic attack. This study provides a theoretical basis for the development of heterogeneous catalytic ozonation systems for PFOA and PFOS treatment.

1. Introduction

Perfluorinated compounds (PFAS) are a class of compounds primarily composed of carbon and fluorine atoms. Due to their unique surfactant properties and thermal stability, they are widely used in various industrial processes such as the production of fire suppressing foams, electroplating, textiles and leather (Ji et al., 2020). Perfluorooctanoic acid (PFOA) and perfluorooctane sulfonic acid (PFOS) are the most common PFAS found in the environment. Due to the presence of numerous stable C—F bonds, they exhibit extremely high chemical and thermal stability (Trojanowicz and Koc, 2013), resisting degradation under natural conditions. The degradation process for PFOA and PFOS involves the cleavage of both C—C and C—F bonds. The cleavage of C—C bonds does not effectively achieve the degradation of PFOA and PFOS, as it produces short-chain perfluorinated compounds. Therefore, the mineralization and defluorination process caused by C—F bond cleavage is crucial for the effective degradation of PFOA and PFOS. Organic pollutants generally exhibit strong hydrophobicity, resulting in low water solubility. However, molecules such as PFOA and PFOS contain hydrophilic groups like sulfonic acid and carboxylic acid, which contribute to their relatively low pK_a values (PFOS: $\text{pK}_a = -3.27$, PFOA: $\text{pK}_a = -0.2$ (Eva and Reinhard, 2008; Goss, 2008) and result in PFOA and PFOS exhibiting a certain degree of water solubility, making them more prone to environmental migration. The widespread occurrence and migration of PFOA and PFOS are of concern as previous studies have shown that these substances are carcinogenic (Vieira et al., 2013), neurotoxic (Mariussen, 2012), genotoxic (Liu et al., 2014) and induce reproductive toxicity (Logeshwaran et al., 2021), with their accumulation throughout the food chain posing a significant threat to human health. Therefore, there is an urgent need to develop effective methods for the treatment and removal of PFOA and PFOS to ensure environmental safety and human health.

In recent years, advanced oxidation processes (AOPs) have been widely used for the treatment of recalcitrant organic pollutants, such as PFOA and PFOS (Guan et al., 2022; Lee et al., 2020). However, the practical application of AOPs has some notable limitations. For example, photocatalysis and electrochemical technologies have high energy consumption requirements and are prone to degradation, resulting in a reduced removal performance, while Fenton-based methods cause secondary pollution due to the addition of metals into the reaction solution (Saravanan et al., 2022). In contrast, catalytic O_3 oxidation technologies are not limited by these issues, as pollutants in water can be degraded via a direct reaction with O_3 molecules or an indirect reaction with reactive oxidative species (e.g., $\cdot\text{OH}$, $\cdot\text{O}_2^-$, $^1\text{O}_2$) generated by O_3 (Yu et al., 2020). To further improve the mass transfer efficiency of O_3 , various physicochemical techniques have been combined with O_3 oxidation systems (Wang and Chen, 2020). Among these techniques, catalysis by transition metals, particularly Fe, has received significant attention due to its easy availability and broad practical applicability (Jothinathan et al., 2022; Shi et al., 2023; Yang et al., 2022). For example, Ouyang et al. (2021) used computational simulations to show that the Fe(III) configuration had a lower reaction barrier as an O_3 catalyst, than the Fe(II) configuration. Furthermore, the addition of Fe (III) can effectively promote the decomposition of O_3 , leading to the generation of more reactive oxidative species. Studies have also

demonstrated that the Lewis acid sites and porosity of Fe-based O_3 catalysts can achieve a higher catalytic activity for pollutant degradation reactions (Song et al., 2022; Yu et al., 2019b). Chen and Wang (2021) utilized a $\text{Co}_3\text{O}_4\text{-C@FeOOH}$ catalyst for the catalytic O_3 oxidation degradation of norfloxacin, showing that the valence state transition between Fe(III) and Fe(II) plays a crucial role in the catalysis of norfloxacin degradation, achieving 100 % degradation within 10 min. Xu et al. (2023) prepared a Fe-Mn-C catalyst for the catalytic O_3 oxidation degradation of ibuprofen, achieving 97 % degradation efficiency within 10 min, while Yu et al. (2019a) prepared a Fe-based O_3 catalyst for the degradation of 4-nitrophenol, achieving 100 % degradation within 30 min.

In this regard, it can be reasonably inferred that the Fe- $\text{Al}_2\text{O}_3/\text{O}_3$ system has good potential for the degradation and defluorination of PFOA and PFOS. However, in existing studies, the mechanism of this system is still not well understood. In fact, the investigation of the reaction sites of ROS and Fe plays an important role in the degradation and defluorination process of PFOA and PFOS (Lee et al., 2020; Yu et al., 2019b). Additionally, using DFT calculations to find specific attack sites of pollutants is of significant importance for the development of selective treatment techniques (Gao et al., 2021).

Therefore, the aim of this study is to comprehensively investigate the degradation and defluorination mechanisms of PFOA and PFOS in the Fe- $\text{Al}_2\text{O}_3/\text{O}_3$ system. Specifically, this study targets to (1) to investigate the influence of different initial pH values, O_3 carrier gas flow rates and catalyst dosages on the PFOA and PFOS defluorination effectiveness of the Fe- $\text{Al}_2\text{O}_3/\text{O}_3$ system; (2) to explore the mechanisms of action of free radicals (such as $\cdot\text{OH}$ and $\cdot\text{O}_2^-$) and non-free radicals (such as $^1\text{O}_2$ and electron transfer) during the processes of PFOA and PFOS defluorination; (3) to elucidate the transformation pathways of PFOA and PFOS by combining DFT theoretical calculations with the identification of degradation products. Overall, the aim of this study was to provide guidance for the development and improvement of catalytic O_3 oxidation treatments for PFOA and PFOS.

2. Materials and methods

2.1. Experimental material

The commercial catalyst Fe- Al_2O_3 was purchased from Shandong Haizhiyan Environmental Technology Co. Ltd. All reagents used were of analytical grade or higher purity, with detailed information on the reagents used provided in the Supplementary Materials (Text S1).

2.2. Characterization analysis

The catalysts elemental composition, surface morphology, crystal structure, surface functional groups, elemental oxidation states and electrochemical properties were analyzed using X-ray fluorescence spectroscopy (ED-XRF, EDX-7000, Shimadzu, Japan), scanning electron microscopy-energy-dispersive X-ray spectroscopy (SEM-EDS, Sigma 300, Zeiss, Germany), X-ray diffraction (XRD, Rigaku, SmartLab, Japan), X-ray photoelectron spectroscopy (XPS, Escalab 250Xi, Thermo Fisher, UK) and an electrochemical workstation (CHI660E, Chen Hua, China). Active oxidation species were identified using an electron paramagnetic

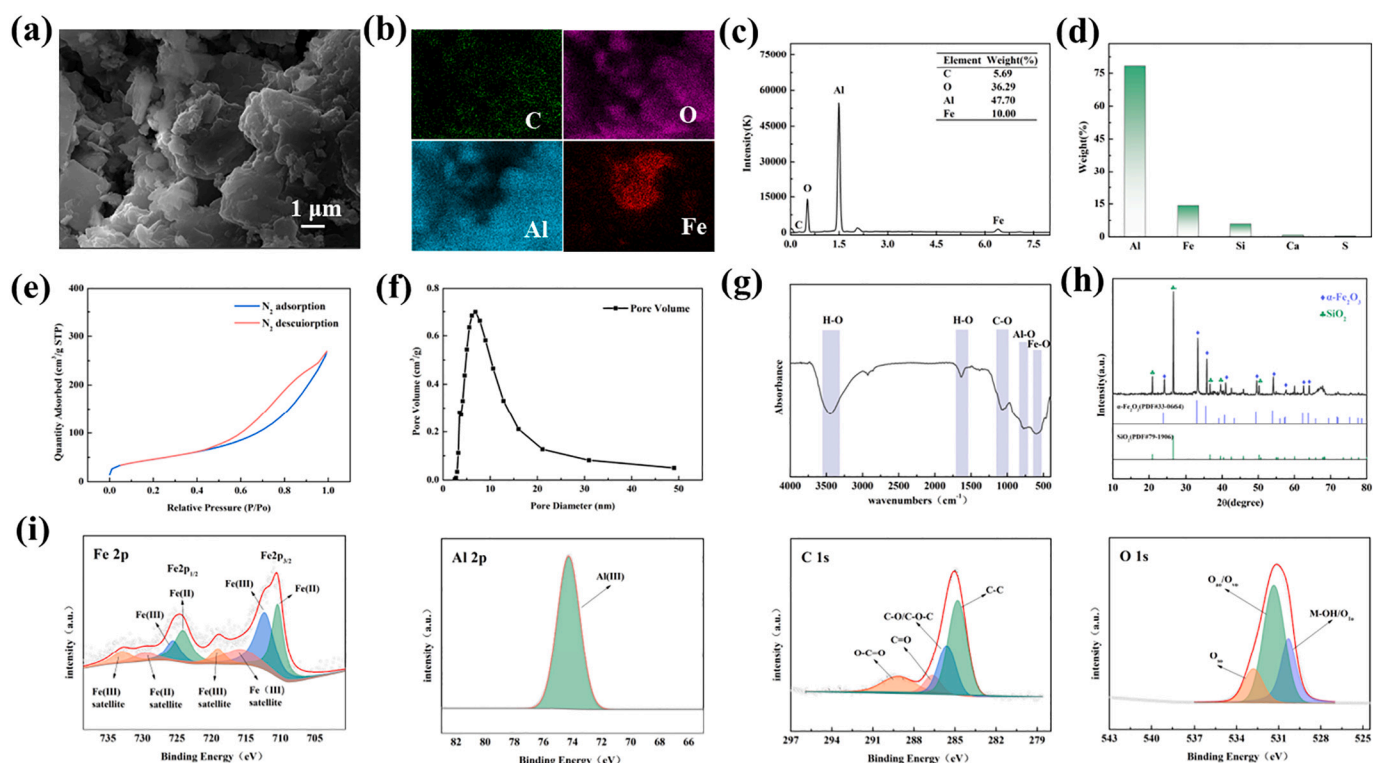


Fig. 1. (a) SEM and (b) EDS images; (c) The proportion of elements identified by EDS and (d) XRF; (e) Adsorption-desorption curve; (f) Aperture distribution; (g) FTIR; (h) XRD; (i) XPS.

resonance spectrometer (EPR, EMXplus-10/12, Bruker, Germany).

2.3. Experimental method

The experiment was conducted at room temperature, in plastic beakers containing 250 mL of solution spiked with an initial concentration of $2.5 \text{ mg}\cdot\text{L}^{-1}$ PFOA or PFOS. The catalyst was added and an O_3 generator was used to evenly disperse O_3 into the solution through an aeration disc at the bottom of the beaker. Samples were collected at designated time intervals and after filtration through a $0.22 \mu\text{m}$ syringe filter membrane, the F^- ion concentration was determined by ion chromatography. The defluorination rate (DeF) of PFOA and PFOS was calculated according to Eq. (1). All experiments and tests were performed in triplicate and the results were expressed as a mean value.

$$\text{DeF} = \frac{F_t}{F_0} \times 100\% \quad (1)$$

Where, DeF represents the defluorination rate; F_t indicates the concentration of inorganic F^- in the solution at a specific time ($\text{mg}\cdot\text{L}^{-1}$); and F_0 represents the initial concentration of organic F^- in the solution ($\text{mg}\cdot\text{L}^{-1}$).

$$\ln \frac{F_0 - F_t}{F_0} = -kt \quad (2)$$

$$\text{SF} = \frac{k_{\text{Fe-Al}_2\text{O}_3/\text{O}_3}}{k_{\text{O}_3} + k_{\text{Fe-Al}_2\text{O}_3}} \quad (3)$$

Where, $k_{\text{Fe-Al}_2\text{O}_3/\text{O}_3}$, k_{O_3} , and $k_{\text{Fe-Al}_2\text{O}_3}(\text{min}^{-1})$ are the first-order kinetic constant of PFOA and PFOS removal under synergetic treatment, solo ozone treatment, and solo $\text{Fe-Al}_2\text{O}_3$ treatment, respectively.

EPR (electron paramagnetic resonance) was used to determine the $\cdot\text{OH}$, $\cdot\text{O}_2^-$ and $^1\text{O}_2$ species in the system following capture by DMPO and TEMP. The contribution of $\cdot\text{OH}$, $\cdot\text{O}_2^-$ and $^1\text{O}_2$ to the defluorination of PFOA and PFOS were calculated through quenching experiments using

$25 \text{ mmol}\cdot\text{L}^{-1}$ TBA, d-BQ and FFA as quenchers for $\cdot\text{OH}$, $\cdot\text{O}_2^-$ and $^1\text{O}_2$, respectively. The presence of Fe(IV) in the system was identified indirectly by monitoring the degradation of PMSO and the formation of PMSO₂. The PFOA and PFOS conversion intermediates formed during the degradation process, were observed via ultra-high resolution quadrupole-Orbitrap mass spectrometry.

2.4. Analytical methods

The F^- concentration in solution was analyzed using an ion chromatograph (ICS-900, DIONEX, America). The conversion intermediates of PFOA and PFOS were analyzed using an ultra-high resolution quadrupole-Orbitrap mass spectrometer (UPLC-Q-Orbitrap HRMS, Thermo Fisher Scientific, China). PMSO and PMSO₂ were analyzed using a liquid chromatograph equipped with a UV detector (Waters Alliance e2695, US). A detailed description of the analytical methods used is provided in the Supplementary Materials (Text S2).

2.5. Theoretical calculation

All calculations were performed using Gaussian v.09 software. The B3LYP method within the density functional theory (DFT) framework was employed to optimize the PFOA and PFOS models at the 6-31G* basis set level, with frequency calculations and analysis conducted based on the optimized structures. The data was visualized using Gauss View v.6 software. The active sites of PFOA and PFOS were determined based on highest occupied molecular orbital (HOMO) and Fukui function calculations (Lu and Chen, 2012, 2022).

2.6. Characterization of Fe-Al₂O₃

The morphology and structure of the $\text{Fe-Al}_2\text{O}_3$ catalyst were analyzed by scanning electron microscopy (SEM), with images revealing a rough, block-like structure at the micro-scale, as shown in Fig. 1a.

Table 1
Fukui index of PFOA.

Atom	q(N)	q(N+1)	q(N-1)	f ⁻	f ⁺	f ⁰	CDD
1(C)	0.2012	0.0656	0.2597	0.0585	0.1356	0.097	0.0771
2(C)	0.1891	0.1436	0.2201	0.031	0.0456	0.0383	0.0146
3(C)	0.18	0.1474	0.1993	0.0194	0.0326	0.026	0.0133
4(C)	0.1797	0.1488	0.2001	0.0204	0.0309	0.0257	0.0105
5(C)	0.1793	0.1504	0.1999	0.0207	0.0289	0.0248	0.0083
6(C)	0.1787	0.1523	0.1991	0.0204	0.0264	0.0234	0.0061
7(C)	0.1765	0.1558	0.1948	0.0183	0.0208	0.0195	0.0025
8(C)	0.278	0.264	0.2916	0.0136	0.0139	0.0138	0.0003
9(O)	-0.2503	-0.397	-0.0734	0.1768	0.1467	0.1618	-0.0301
10(O)	-0.1499	-0.2317	-0.0787	0.0712	0.0818	0.0765	0.0106
11(F)	-0.0941	-0.1401	-0.0486	0.0456	0.046	0.0458	0.0004
12(F)	-0.0967	-0.14	-0.043	0.0537	0.0433	0.0485	-0.0104
13(F)	-0.0949	-0.125	-0.0637	0.0313	0.03	0.0306	-0.0012
14(F)	-0.0875	-0.1162	-0.0514	0.0361	0.0287	0.0324	-0.0074
15(F)	-0.0899	-0.1176	-0.0547	0.0352	0.0277	0.0315	-0.0074
16(F)	-0.0913	-0.1186	-0.0546	0.0367	0.0273	0.032	-0.0093
17(F)	-0.0908	-0.1161	-0.0561	0.0347	0.0253	0.03	-0.0095
18(F)	-0.0896	-0.1141	-0.0527	0.0368	0.0245	0.0307	-0.0123
19(F)	-0.0905	-0.1153	-0.0564	0.0341	0.0248	0.0295	-0.0093
20(F)	-0.0917	-0.1136	-0.0555	0.0361	0.022	0.029	-0.0142
21(F)	-0.0912	-0.1127	-0.0607	0.0305	0.0215	0.026	-0.009
22(F)	-0.0916	-0.1099	-0.0575	0.034	0.0183	0.0262	-0.0158
23(F)	-0.0888	-0.112	-0.0609	0.0279	0.0232	0.0256	-0.0047
24(F)	-0.0907	-0.1045	-0.0711	0.0196	0.0139	0.0167	-0.0058
25(F)	-0.091	-0.1046	-0.0692	0.0217	0.0136	0.0177	-0.0081
26(H)	0.2078	0.1612	0.2436	0.0358	0.0466	0.0412	0.0108

Elemental distribution analysis of the Fe-Al₂O₃ catalyst was performed using energy-dispersive X-ray spectroscopy (EDS), with the results shown in Fig. 1b-c. Preliminary results indicated that aluminum (Al) was the major constituent element of the Fe-Al₂O₃ catalyst, while combined analysis of the SEM and EDS images, showed that iron (Fe) was irregularly embedded within the Al₂O₃ matrix. The results of elemental composition analysis by X-ray fluorescence (XRF) are shown in Fig. 1d, further demonstrating that Al was the main element in the Fe-Al₂O₃ catalyst, which is consistent with the results of EDS analysis.

The specific surface area of the Fe-Al₂O₃ catalyst was measured and calculated using a physical adsorption instrument, with the results shown in Fig. 1e-f and Supplementary Materials (Table S1). The nitrogen adsorption-desorption isotherm exhibited a hysteresis loop, indicative of a type IV isotherm, suggesting that the Fe-Al₂O₃ catalyst possesses a mesoporous structure. The average specific surface area, average pore volume and average pore diameter of the Fe-Al₂O₃ catalyst are presented in Table 1, showing that the pore sizes were mainly distributed in the range of 1–10 nm, further indicating a mesoporous structure (Guan et al., 2022). This finding is consistent with the results obtained from the nitrogen adsorption-desorption isotherm.

The surface functional groups of the Fe-Al₂O₃ catalyst were analyzed by Fourier-transform infrared spectroscopy (FTIR), with the results

shown in Fig. 1g. Absorption peaks were observed at around 3453 cm⁻¹ and 1637 cm⁻¹, corresponding to the vibration and stretching of H—O bonds (Guan et al., 2020); a peak at around 587 cm⁻¹ was attributed to the vibration and stretching of Fe—O bonds (Wu et al., 2021); peaks at around 7770 cm⁻¹ were assigned to the vibration and stretching of Al—O bonds (Zhou et al., 2022); peaks observed around 1081 cm⁻¹ indicated the vibration and stretching of C—O bonds (Liu et al., 2020). The results of FTIR analysis indicated the abundant presence of oxygen-containing functional groups on the Fe-Al₂O₃ catalyst, such as hydroxyl groups, ethers and carboxyl groups (Wang et al., 2020), which play a crucial role in promoting the catalytic oxidation of O₃ and organic pollutants (Song et al., 2019).

XRD analysis was conducted to examine the crystalline phase and structural composition of the Fe-Al₂O₃ catalyst (Fig. 1h). Results revealed that the characteristic diffraction peaks of the Fe-Al₂O₃ catalyst matched those of the standard reference cards of SiO₂ (PDF#79–1906) and α-Fe₂O₃ (PDF#33–0664) (Mahajan and Jeevanandam, 2018). However, no diffraction peaks corresponding to Al₂O₃ were observed during XRD analysis, which was attributed to the core-shell structure of the Fe-Al₂O₃ catalyst. The active metallic elements were located in the shell layer, while Al was located in the core layer, leading to the undetectability of Al in the core layer during analysis.

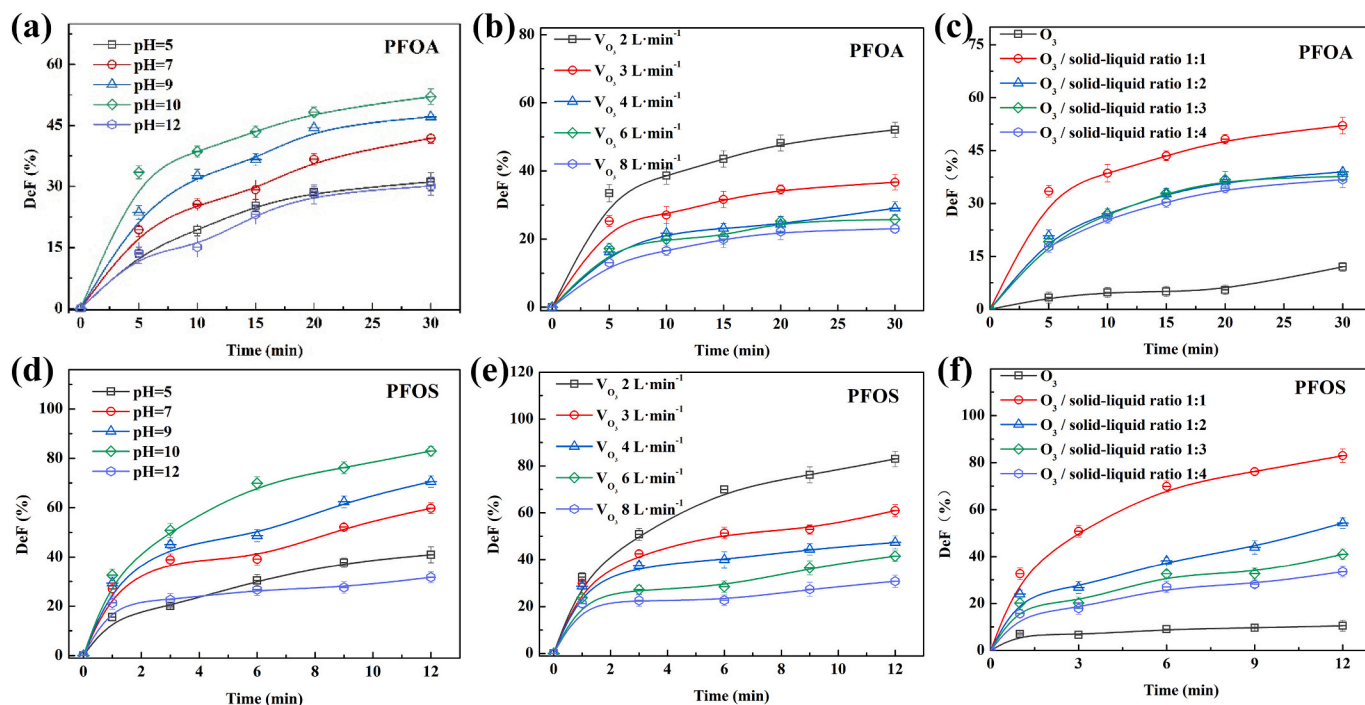


Fig. 2. (a), (d) Effects of different initial pH values on PFOA and PFOS defluorination, respectively; (b), (e) Effects of different O₃ carrier gas flow rates on PFOA and PFOS defluorination, respectively; (c), (f) Effects of different catalyst dosages on PFOA and PFOS defluorination, respectively.

XPS analysis was conducted to examine the surface elemental composition and oxidation states of the Fe-Al₂O₃ catalyst (Fig. 1i). The results of XPS analysis identified the main metallic elements as Fe, Al, C and O, with Fe 2p peaks observed at binding energies of 710.5 and 724.4 eV, corresponded to the Fe 2p_{3/2} and Fe 2p_{1/2} orbitals. By fitting the Fe 2p XPS spectra, the peaks located at 710.3, 712.2, 724.1 and 725.5 eV were assigned to Fe(II) 2p_{3/2}, Fe(III) 2p_{3/2}, Fe(II) 2p_{1/2} and Fe(III) 2p_{1/2}, respectively (He et al., 2023). The peak of Al 2p at a binding energy of 74.5 eV was assigned to Al—O bonds (Guan et al., 2022). By fitting the C 1s XPS spectra, the peak positions located at 284.8, 285.6, 286.7 and 289.2 eV were assigned to C—C, C—O—C/C—O, C=O, and O—C=O (Chella et al., 2015), while the peaks in the O 1s XPS spectra at 530.6, 531.7 and 532.9 eV were assigned to metal hydroxyl oxygen (M—OH) or lattice oxygen (O_{lo}), surface-adsorbed oxygen (O_{ao}) or oxygen vacancies (O_{vo}) and surface hydroxyl oxygen (O_{so}) (Bing et al., 2015; Guan et al., 2022). Overall, the results of XPS analysis indicate the presence of mixed-valence Fe and an abundance of oxygen-containing functional groups in the Fe-Al₂O₃ catalyst. The process of redox cycling by metals between different oxidation states, has a positive effect on the catalysis of O₃ oxidation to generate active oxygen species (Lai et al., 2019). Furthermore, the abundance of oxygen-containing functional groups also enhances the catalytic performance of the Fe-Al₂O₃ catalyst. These findings are consistent with the results of FTIR analysis.

3. Results and discussion

3.1. Effect of reaction condition parameters

3.1.1. Effect of initial solution pH on PFOA and PFOS defluorination

The influence of the initial solution pH on the PFOA and PFOS defluorination efficiency of the system was investigated within an initial pH range of 5.0 to 12.0, with the result presented in Fig. 2a and d. Within the initial pH range of 5–10, both PFOA and PFOS defluorination rates increased under higher initial pH conditions. The optimal defluorination efficiency was achieved at pH 10.0, with a PFOA defluorination rate of 52.07 % after 30 min and a PFOS defluorination rate of 82.97 % after 12 min. However, further increase in the initial pH to 12, resulted in the

PFOA and PFOS defluorination rates decreasing sharply. Possible reasons for this phenomenon are as follows: 1) Under acidic conditions, O₃ directly reacts with pollutants in their molecular state (Zhang et al., 2019a); 2) Under alkaline conditions, the surface electron density of the catalyst is higher than under acidic conditions (Zhang et al., 2021). 3) Due to the electrophilic nature of O₃ (Gardoni et al., 2012), O₃ molecules are more easily adsorbed by the catalyst under alkaline conditions. Through activation and decomposition on the catalyst's surface active sites (such as electron-rich oxygen-containing groups) (Zhang et al., 2021), O₃ molecules can undergo chain decomposition reactions to produce active oxygen species (Garcia-Ballesteros et al., 2019; Zoumpouli et al., 2020), leading to more efficient pollutant degradation. However, the defluorination rates of PFOA and PFOS sharply decrease at an initial pH of 12. We speculate that the reason is that pH 12 belongs to strong alkaline conditions, and studies have shown that under strong alkaline conditions, ozone decomposition is inhibited. Additionally, CO₃²⁻ produced in strong alkaline systems quenches and clears •OH (Alatona et al., 2002; Khuntia et al., 2015), leading to a decrease in the defluorination rates of PFOA and PFOS.

3.1.2. Effect of O₃ carrier gas flow on PFOA and PFOS defluorination

The influence of O₃ carrier gas flow rate on the defluorination efficiency of PFOA and PFOS was investigated in the range of 2 to 8 L·min⁻¹, with the results presented in Fig. 2b and e. Results show that the O₃ carrier gas flow rate was negatively correlated with the defluorination rates of both PFOA and PFOS. The optimal defluorination performance for both PFOA and PFOS was achieved at an O₃ carrier gas flow rate of 2 L·min⁻¹, achieving a PFOA defluorination rate of 52.07 % after 30 min and a PFOS defluorination rate of 82.97 % after 12 min. The negative correlation between the defluorination rates of both PFOA and PFOS and the O₃ carrier gas flow rate can potentially be attributed to two factors. Firstly, previous research has shown that a negative correlation exists between O₃ concentrations and the carrier gas flow rate, with increasing carrier gas flow rates leading to a decrease in the generated O₃ concentration (Guan et al., 2020) and subsequently, lower O₃ concentrations participating in the reaction system. Secondly, when the gas flow rate was excessively high, the contact time between O₃ and

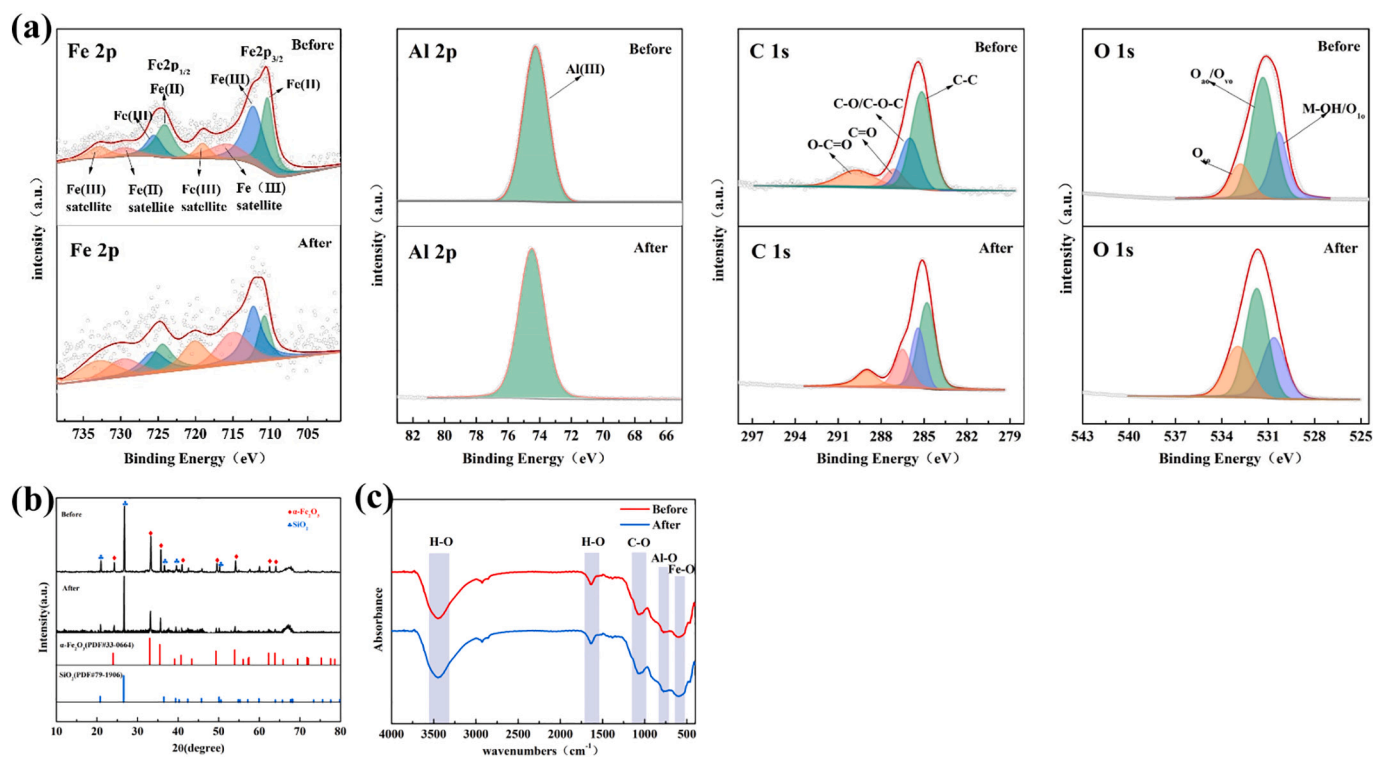


Fig. 3. (a) XPS Fe 2p, Al 2p, C1s and O 1s spectra of Fe-Al₂O₃ before and after the reaction; (b) XRD spectra of Fe-Al₂O₃ before and after the reaction; (c) FTIR spectra of Fe-Al₂O₃ before and after the reaction.

the catalyst or the solution is reduced. O₃ molecules that are not promptly adsorbed by the catalyst escape from the reaction system, leading to a decrease in the O₃ utilization efficiency and incomplete reaction progression (Guan et al., 2020).

3.1.3. Effect of catalyst dosage on PFOA and PFOS defluorination

The influence of catalyst dosage on the defluorination efficiency of PFOA and PFOS was investigated, at varying solid-liquid ratios of catalyst to liquid volume ranging from 1:1 to 1:4 (Fig. 2c and f). Results showed that the catalyst dosage was positively correlated with the defluorination rates of both PFOA and PFOS, with the optimal defluorination efficiency achieved at a solid-liquid ratio of 1:1. Under optimal conditions, a PFOA defluorination rate of 52.07 % was reached after 30 min and a PFOS defluorination rate of 82.97 % was reached after 12 min. The addition of a catalyst significantly improved the defluorination rates of both PFOA and PFOS in the reaction system, with a solid-liquid ratio of 1:1 resulting in a 2.32-fold higher PFOA defluorination rate as compared to the O₃-oxidation system, while the PFOS defluorination rate was 5.92-fold higher than the O₃-oxidation system. The catalyst dosage was found to be positively correlated to the defluorination rates of both PFOA and PFOS, which was speculated to be due to two factors. Firstly, the adsorption of O₃ by the catalyst prolongs the contact time between O₃ and the liquid phase in the system, facilitating the decomposition of O₃ molecules, generating reactive oxidative species (Garcia-Ballesteros et al., 2019; Zoumpouli et al., 2020) and promoting the defluorination of PFOA and PFOS. Secondly, previous research has shown that as a catalytically active metal, α-Fe₂O₃, can effectively enhance the generation of reactive oxidative species within the system (Kohantorabi et al., 2022; Liang et al., 2023), which is beneficial to the defluorination of PFOA and PFOS.

3.2. Mechanistic analysis

3.2.1. Catalytic mechanism analysis

a Analysis of reaction sites

XPS analysis results of the Fe-Al₂O₃ catalyst before and after multiple cycles of use (Fig. 3a), showed that the proportions of Fe²⁺ and Fe³⁺ before the reaction were 50.6 % and 49.4 %, while after the reaction the relative proportions were 42.5 % and 57.5 %, indicating that a small portion of Fe²⁺ was converted to Fe³⁺ during the reaction. The proportions of C—C, C-O-C/C-O, C=O and O-C=O functional groups before the reaction were 53 %, 24.8 %, 7.8 % and 14.4 %, respectively, while after the reaction their proportions were 45.3 %, 23.7 %, 19.9 % and 11.6 %, respectively, showing a change in certain carbon functional group structures during the reaction. The proportions of M-OH or O_{1s}, O₂ or O_{2s}, and O_{3s} functional groups before the reaction were 28.6 %, 56.5 % and 14.9 %, while after the reaction their proportions were 29.1 %, 46.5 % and 24.4 %, indicating changes in certain oxygen-containing functional group structures during the reaction process. In summary, the elements Fe, C and O all played significant roles in the catalytic process.

A comparison of the catalysts XRD spectra before and after use (Fig. 3b), showed that the elemental diffraction peak signals weakened slightly after use, indicating degradation of the catalyst materials structure due to gas and liquid flow. Although some loss in catalytic performance was observed with use, the overall change in activity was not significant, suggesting that the surface lattice structure of the catalyst was relatively stable. A comparison of the FTIR results for the catalyst before and after use (Fig. 3c), shows a reduction in the abundance of functional groups after use, indicating the involvement of oxygen-containing functional groups in the catalytic process. In conclusion, C and O functional groups and the variable valence metal Fe are important reaction sites for the catalytic process.

b Identification of active oxides

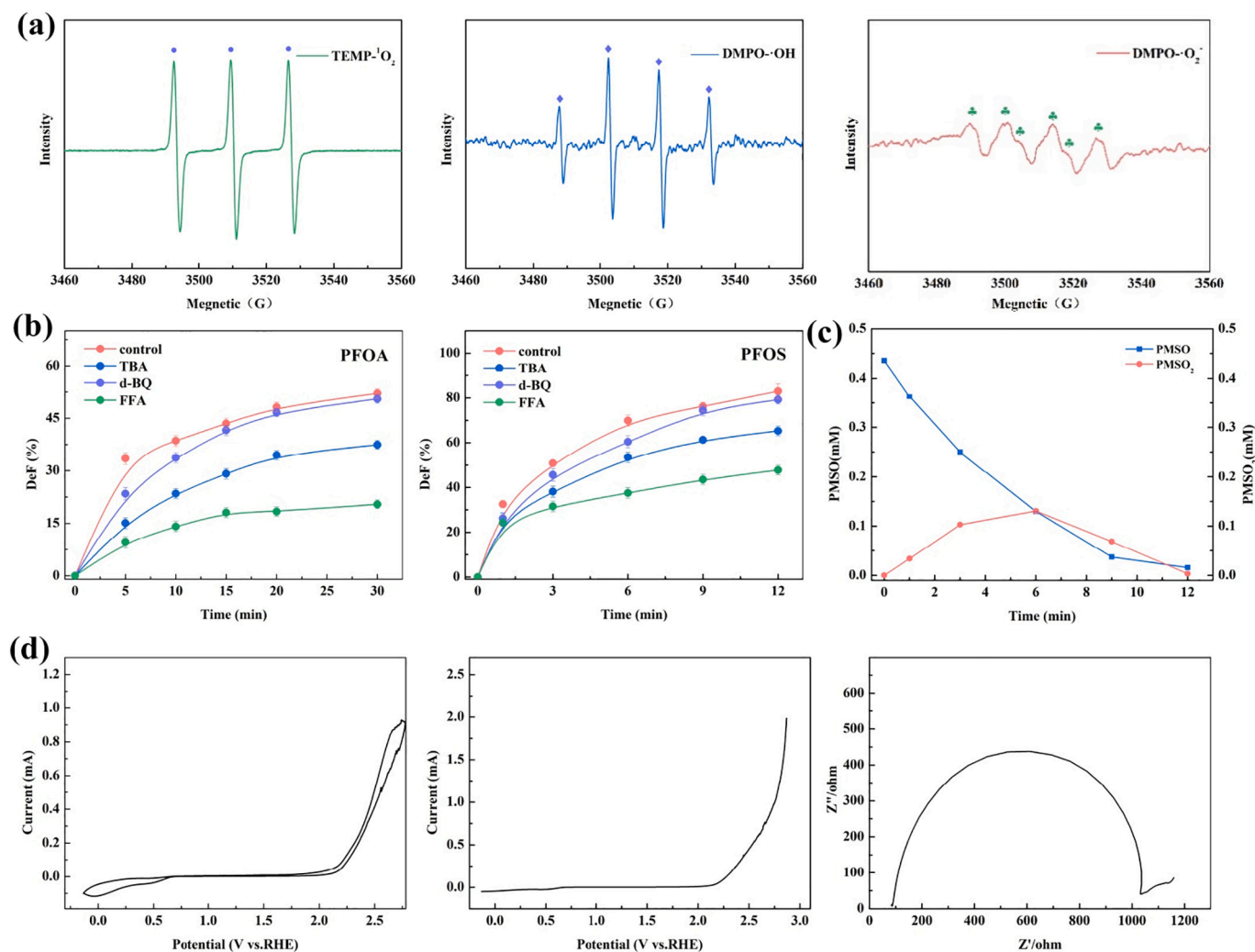


Fig. 4. (a) EPR spectra of ¹O₂, •OH and •O₂⁻ in the Fe-Al₂O₃/O₃ system; (b) Quenching test results in the Fe-Al₂O₃/O₃ system; (c) PMSO degradation and PMSO₂ generation curve for the Fe-Al₂O₃/O₃ system; (d) CV, LSV and EIS curves for Fe-Al₂O₃.

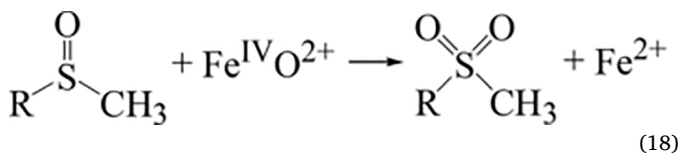
The possible reactive oxygen species within the system were identified through EPR, with the results shown in Fig. 4a. The system exhibited characteristic signal peaks of 1:1:1 for ¹O₂, 1:2:2:1 for •OH and 1:1:1:1 for •O₂⁻ (Guan et al., 2022), confirming the presence of ¹O₂, •OH and •O₂⁻ in the system, with peak intensities following the ranked order of ¹O₂ > •OH > •O₂⁻. The reactive oxygen species generation pathways are shown in Eqs. (4)–(16), in which O₃ self-decomposes with water to generate •OH, initiating a free radical chain reaction that gradually generates ¹O₂ and •O₂⁻. The contribution of each reactive oxygen species to the defluorination of PFOA and PFOS was explored through quenching experiments, allowing the specific contribution rates of each reactive species to be calculated according to Eq. (17). As shown in Fig. 4b, the PFOA defluorination rate decreased by 14.64 %, 1.54 % and 31.64 % when TBA, d-BQ and FFA were added, respectively, while the PFOS defluorination rate decreased by 17.68 %, 3.75 % and 35.23 %, respectively. These results indicate that during the process of PFOA and PFOS defluorination, the contribution of each reactive oxygen species followed the ranked order of ¹O₂ > •OH > •O₂⁻, which was consistent with the results of EPR. However, previous research has indicated that the defluorination of PFOA and PFOS does not solely rely on the activity of ¹O₂, •OH and •O₂⁻, with other reactive species or processes potentially involved in the defluorination reaction. For example, studies have shown that electron transfer plays an important role in the degradation of pollutants such as PFOA and PFOS by advanced oxidation processes (Huang et al., 2016; Kong et al., 2022; Li et al., 2022b). Considering the

characteristics of this catalyst, it may be speculated that an electron transfer pathway exists within the system and this possibility will be explored further in the following discussion.



Table 2
Fukui index of PFOS.

Atom	q(N)	q(N+1)	q(N-1)	f ⁻	f ⁺	f ⁰	CDD
1(C)	0.1792	0.1346	0.2093	0.0301	0.0446	0.0374	0.0146
2(C)	0.1776	0.1377	0.1973	0.0196	0.0399	0.0298	0.0203
3(C)	0.1797	0.1386	0.1992	0.0196	0.0411	0.0303	0.0215
4(C)	0.1794	0.1407	0.1993	0.0199	0.0387	0.0293	0.0188
5(C)	0.1794	0.1441	0.1995	0.0201	0.0354	0.0277	0.0153
6(C)	0.1789	0.1486	0.1988	0.0199	0.0303	0.0251	0.0104
7(C)	0.1767	0.154	0.1948	0.0181	0.0227	0.0204	0.0046
8(C)	0.2781	0.2634	0.2915	0.0134	0.0147	0.0141	0.0014
9(S)	0.5158	0.4572	0.5671	0.0513	0.0586	0.0549	0.0073
10(O)	-0.2814	-0.3554	-0.1832	0.0982	0.074	0.0861	-0.0243
11(O)	-0.2961	-0.3408	-0.2147	0.0814	0.0448	0.0631	-0.0366
12(O)	-0.1841	-0.2295	-0.1407	0.0434	0.0455	0.0444	0.0021
13(F)	-0.0729	-0.1073	-0.0295	0.0434	0.0344	0.0389	-0.009
14(F)	-0.0778	-0.1107	-0.0337	0.0442	0.0329	0.0385	-0.0113
15(F)	-0.0812	-0.1163	-0.0481	0.0331	0.0351	0.0341	0.002
16(F)	-0.0927	-0.122	-0.0651	0.0275	0.0293	0.0284	0.0018
17(F)	-0.089	-0.1219	-0.0563	0.0328	0.0329	0.0328	0.0001
18(F)	-0.0867	-0.12	-0.0548	0.0319	0.0333	0.0326	0.0014
19(F)	-0.0876	-0.1191	-0.0538	0.0339	0.0315	0.0327	-0.0024
20(F)	-0.0898	-0.1211	-0.058	0.0319	0.0313	0.0316	-0.0005
21(F)	-0.0895	-0.1177	-0.0546	0.0349	0.0282	0.0315	-0.0067
22(F)	-0.089	-0.1194	-0.0553	0.0337	0.0304	0.0321	-0.0033
23(F)	-0.0901	-0.1148	-0.055	0.0351	0.0247	0.0299	-0.0104
24(F)	-0.09	-0.1176	-0.0573	0.0328	0.0276	0.0302	-0.0052
25(F)	-0.0915	-0.1112	-0.0583	0.0332	0.0197	0.0265	-0.0135
26(F)	-0.0906	-0.1141	-0.0605	0.0302	0.0234	0.0268	-0.0067
27(F)	-0.0902	-0.1048	-0.0711	0.0191	0.0146	0.0168	-0.0046
28(F)	-0.0902	-0.1047	-0.0688	0.0214	0.0146	0.018	-0.0068
29(F)	-0.0879	-0.1125	-0.0607	0.0272	0.0246	0.0259	-0.0026
30(H)	0.2036	0.1622	0.2224	0.0188	0.0414	0.0301	0.0226



3.2.2. Degradation and defluorination mechanism analysis

The highest occupied molecular orbital (HOMO) and Fukui functions of PFOA and PFOS were calculated using the DFT method. The HOMO can be used to characterize the electron-donating capability of pollutants, while the Fukui indices f^+ , f^- and f^0 , represent nucleophilic, electrophilic and radical activity, respectively, with larger values indicating higher reactivity (Niu et al., 2013; Zhang et al., 2019b). The ground-state charge density difference (CDD) reflects the electrophilic and nucleophilic properties of an atom, where a higher CDD value implies a greater susceptibility to nucleophilic attack, while a lower value

suggests a higher susceptibility to electrophilic attack (Gao et al., 2021). The calculation results presented in Fig. 5a, Table 1, Table 2 and Fig. S1 (Supplementary Materials), show that the HOMO overlap of PFOS was larger than that of PFOA, indicating that PFOS is more susceptible to electron transfer and attack from its surroundings. For PFOA, C(1), O(9), O(10), F(11), F(12), F(16) and F(18) were found to have relatively higher f^- values, suggesting that these sites are more susceptible to electrophilic attack leading to electron transfer, decarboxylation and defluorination reactions. In addition, sites C(1), C(2), C(3), O(9), O(10), F(11), F(12) and H(26) exhibited larger f^+ values, indicating that these sites are more prone to nucleophilic attack resulting in carbon-carbon bond cleavage, decarboxylation and defluorination reactions. C(1), C(2), O(10), F(11), F(12) and H(26) had larger f^0 values, suggesting that these sites were more susceptible to radical attack leading to decarboxylation. Similarly, PFOS was also found to be able to undergo electron transfer, carbon-carbon bond cleavage, desulfonation and defluorination reactions through electrophilic, nucleophilic and radical

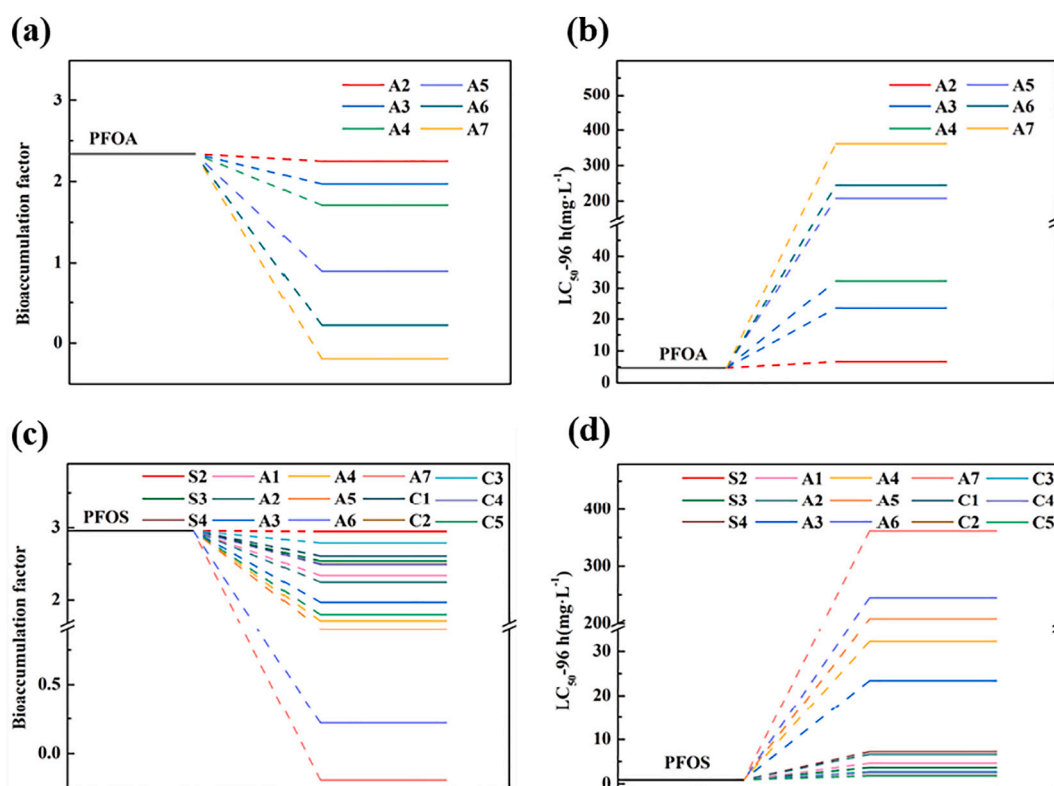


Fig. 6. Bioconcentration factors and $LC_{50-96\text{ h}}$ values (in the fathead minnow) for (a), (b) PFOA and PFOA intermediates; and (c), (d) PFOS and PFOS intermediates in the Fe- Al_2O_3/O_3 system.

attack. CDD value analysis indicated that the sulfonic acid group of PFOS was more susceptible to electrophilic attack than the carboxylic acid group of PFOA, while the α -C of PFOA was more susceptible to nucleophilic attack than the α -C of PFOS.

This study employed LC-MS/MS for the qualitative detection of intermediate products of PFOA and PFOS degradation in this system. Based on the experimental results and the analysis of relevant literature, it may be preliminarily speculated that the intermediate products of PFOA mainly include six short-chain perfluorocarboxylic acids, while the intermediate products of PFOS mainly include three perfluorosulfonic acids, seven perfluorocarboxylic acids and five perfluoroalkanes. A complete list of the specific substances are presented in Table S2 (Supplementary Materials) and the degradation and defluorination pathways are illustrated in Fig. 5b.

It may be speculated that PFOA can undergo two degradation pathways: 1) The formation of short-chain perfluorocarboxylic acids: PFOA is initially adsorbed to the catalyst surface (rich in oxygen groups) through -COO- bonds and undergoes direct electron transfer with the catalyst surface via ROS to form $C_7F_{15}COO^*$ (Fu et al., 2022). Nucleophilic substitution results in Kolbe decarboxylation, generating $C_7F_{15}^*$ (Yang et al., 2023), which further reacts with $\cdot OH$ to form the unstable molecule $C_7F_{15}OH$, which then undergoes defluorination to form $C_6F_{13}COF$. Subsequent hydrolysis and defluorination leads to the formation of $C_6F_{13}COOH$ (Guo et al., 2022; Kundu and Radian, 2022), with further degradation of $C_6F_{13}COOH$ occurring via similar pathways to form shorter-chain perfluorocarboxylic acids. 2) Mineralization into CO_2 and F^- : $C_7F_{15}^*$ is formed from the Kolbe decarboxylation of PFOA, which then reacts with $\cdot OH$ or 1O_2 to generate $C_7F_{15}O^*$, with further decomposition into $C_6F_{13}^*$ and COF_2 . COF_2 can be easily hydrolyzed to CO_2 and F^- , while $C_6F_{13}^*$ participates in subsequent reactions generating shorter-chain perfluoroalkyl radicals, eventually leading to the formation of CO_2 and F^- through mineralization (Fu et al., 2022).

It may be speculated that PFOS can undergo four degradation pathways: 1) Formation of short-chain perfluorosulfonic acids: PFOS is

first adsorbed to the oxygen group rich surface of the catalyst through - SO_3^- bonds, followed by $\cdot SO_3^-$ removal to form $C_8F_{17}^*$, which then reacts with $\cdot OH$ to generate $C_8F_{17}OH$ and subsequently, undergoes defluorination to form $C_7F_{15}COF$. Further hydrolysis and defluorination lead to the formation of $C_7F_{15}COOH$, which forms $C_7F_{15}^*$ after electron transfer and Kolbe decarboxylation, before finally reacting with $\cdot SO_3^-$ to regenerate short-chain perfluorosulfonic acids (Kim et al., 2019; Li et al., 2022a; Yang et al., 2021). 2) Formation of short-chain perfluorocarboxylic acids: As described for the PFOA degradation pathway, PFOS can also generate short-chain perfluorocarboxylic acids. 3) Mineralization into CO_2 and F^- : As described for the PFOA degradation pathway, PFOS can also undergo mineralization into CO_2 and F^- . 4) Formation of perfluoroalkanes: PFOS undergoes desulfonation and C-F bond cleavage, followed by intramolecular free radical cyclization to form perfluoroalkanes (Singh et al., 2019). Further removal of - CF_2 - leads to the formation of C_4F_8 . Previous studies have shown that PFOA and PFOS degradation and defluorination pathways involve the stepwise removal of - CF_2 - (Bruton and Sedlak, 2018; Kim et al., 2019; Saleh et al., 2017), which is consistent with the results of theoretical calculations in the present study and the inferred degradation pathways.

3.2.3. Synergistic effects analysis

To explore the synergistic defluorination effect of Fe- Al_2O_3/O_3 on PFOA and PFOS, the concept of synergistic factor (SF) was introduced (Liang et al., 2021; Sun et al., 2023). It is generally believed that when the synergy factor is greater than 1, the synergy effect is better. According to Eqs. 2–3, it can be calculated that the synergistic factor of Fe- Al_2O_3/O_3 for defluorination of PFOA is 4.25, and for defluorination of PFOS is 10.26 (Table S4). The synergistic factors are all greater than 1, indicating that Fe- Al_2O_3/O_3 has a strong synergistic effect on the defluorination of PFOA and PFOS.

3.3. Toxicity evaluation

Using the Toxicity Estimation Software Tool (T.E.S.T.), six major PFOA intermediates and fifteen major PFOS intermediates were evaluated in terms of their toxicity. The evaluation criteria included the bioconcentration factor (BCF) and acute aquatic toxicity (LC₅₀₋₉₆ h) to the fathead minnow. As shown in Fig. 6, the BCF values for PFOA and PFOS were 2.34 and 2.96 (Fig. 6a and c), indicating that both have a high bioaccumulation potential. The predicted LC₅₀₋₉₆ h values for PFOA and PFOS were 4.66 mg·L⁻¹ and 0.91 mg·L⁻¹, respectively (Fig. 6b and d), indicating a high degree of aquatic toxicity. After the reaction, both the BCF values and the acute aquatic toxicity of PFOA and PFOS decreased significantly, indicating that during the reaction process they were gradually transformed into substances with a lower bioaccumulation potential and toxicity. These findings suggest a significant reduction in ecological risk following treatment. In conclusion, the Fe-Al₂O₃/O₃ system is a safe, sustainable and effective method for the treatment of PFOA and PFOS.

4. Conclusions

The optimal conditions for PFOA and PFOS defluorination using the Fe-Al₂O₃/O₃ system were found to consist of an initial pH of 10, with a carrier gas flow rate of 2 L·min⁻¹ and a solid-to-liquid ratio of 1:1. Under these conditions, the PFOA defluorination rate reached 52.07 %, while the PFOS defluorination rate reached 82.97 %. The Fe-Al₂O₃/O₃ system was found to contain ROS and Fe(IV), which serve as crucial substances and sites for catalysis and the degradation of pollutants. Based on the results of catalyst characterization, DFT calculations and the identification of intermediate products, it may be speculated that PFOA mainly undergoes Kolbe decarboxylation and alcoholization to generate short-chain perfluorocarboxylic acids, while PFOS mainly undergoes desulfonation, Kolbe decarboxylation and alcoholization to produce short-chain perfluorosulfonic acids and perfluorocarboxylic acids. Molecular intramolecular radical cyclization led to the formation of perfluoroalkanes. During the reaction process, the synergistic oxidation effects of both radical and non-radical species promoted the degradation and defluorination of PFOA and PFOS.

CRediT authorship contribution statement

Yumin Zhang: Writing – original draft, Methodology, Investigation, Formal analysis, Data curation, Conceptualization. **Zhijie Guan:** Visualization, Validation, Supervision, Project administration, Conceptualization. **Xiaojian Liao:** Writing – review & editing, Visualization, Validation. **Yu Huang:** Writing – review & editing, Resources, Investigation. **Zhenhua Huang:** Writing – review & editing, Resources, Investigation. **Zhihua Mo:** Writing – review & editing, Resources, Investigation. **Baixuan Yin:** Writing – review & editing, Resources, Investigation. **Xingfan Zhou:** Writing – review & editing, Resources, Investigation. **Wencan Dai:** Visualization, Validation, Supervision, Project administration, Conceptualization. **Jialin Liang:** Validation, Conceptualization. **Shuiyu Sun:** Visualization, Validation, Supervision, Project administration, Conceptualization.

Declaration of competing interest

The authors declare that they have no known competing financial interests or personal relationships that could have appeared to influence the work reported in this paper.

Data availability

Data will be made available on request.

Acknowledgments

The authors acknowledge the financial support of this study by the National Natural Science Foundation of China (No. 42277220), Guangdong Youth Innovative Talent Project (Natural Science) 2023KQNCX204 and National Natural Science Foundation of China (42307520). Furthermore, we also wish to thank the Analysis and Test Center, Guangdong University of Technology for offering the test.

Appendix A. Supplementary data

Supplementary data to this article can be found online at <https://doi.org/10.1016/j.scitotenv.2023.169675>.

References

- Afzal, S., Qian, X., Zhang, J., 2017. High surface area mesoporous nanocast LaMO₃ (M = Mn, Fe) perovskites for efficient catalytic ozonation and an insight into probable catalytic mechanism. *Appl. Catal. B Environ.* 206, 692–703.
- Alatona, I.A., Balcioglu, I.A., Bahnemann, D.W., 2002. Advanced oxidation of a reactive dye bath effluent: comparison of O₃, H₂O₂/UV-C and TiO₂/UV-A processes. *Water Res.* 36, 1143–1154.
- Bing, J., Hu, C., Nie, Y., Yang, M., Qu, J., 2015. Mechanism of catalytic ozonation in Fe₂O₃/Al₂O₃@SBA-15 aqueous suspension for destruction of ibuprofen. *Environ. Sci. Technol.* 49, 1690–1697.
- Bruton, T.A., Sedlak, D.L., 2018. Treatment of perfluoroalkyl acids by heat-activated persulfate under conditions representative of in situ chemical oxidation. *Chemosphere* 206, 457–464.
- Chella, S., Kollu, P., Komarala, E.V.P.R., Doshi, S., Saranya, M., Felix, S., et al., 2015. Solvothermal synthesis of MnFe₂O₄-graphene composite—investigation of its adsorption and antimicrobial properties. *Appl. Surf. Sci.* 327, 27–36.
- Chen, H., Wang, J., 2021. MOF-derived Co₃O₄-C@FeOOH as an efficient catalyst for catalytic ozonation of norfloxacin. *J. Hazard. Mater.* 403, 123697.
- Chen, Z., Chen, W., Liao, G., Li, X., Wang, J., Tang, Y., et al., 2022. Flexible construct of N vacancies and hydrophobic sites on g-C₃N₄ by F doping and their contribution to PFOA degradation in photocatalytic ozonation. *J. Hazard. Mater.* 428, 128222.
- Chen, W., He, H., Liang, J., Wei, X., Li, X., Wang, J., et al., 2023. A comprehensive review on metal based active sites and their interaction with O₃ during heterogeneous catalytic ozonation process: types, regulation and authentication. *J. Hazard. Mater.* 443, 130302.
- Eva, S.-D., Reinhard, M., 2008. Nanofiltration for trace organic contaminant removal: structure, solution, and membrane fouling effects on the rejection of perfluorochemicals. *Environ. Sci. Technol.* 42, 5292–5297.
- Fu, S., Zhang, Y., Xu, X., Dai, X., Zhu, L., 2022. Peroxymonosulfate activation by iron self-doped sludge-derived biochar for degradation of perfluorooctanoic acid: a singlet oxygen-dominated nonradical pathway. *Chem. Eng. J.* 450, 137953.
- Gao, X., Chen, J., Che, H., Ao, Y., Wang, P., 2021. Rationally constructing of a novel composite photocatalyst with multi charge transfer channels for highly efficient sulfamethoxazole elimination: mechanism, degradation pathway and DFT calculation. *Chem. Eng. J.* 426, 131585.
- Garcia-Ballesteros, S., Mora, M., Vicente, R., Vercher, R.F., Sabater, C., Castillo, M.A., et al., 2019. A new methodology to assess the performance of AOPs in complex samples: application to the degradation of phenolic compounds by O₃ and O₃/UV-A-Vis. *Chemosphere* 222, 114–123.
- Gardoni, D., Vailati, A., Canziani, R., 2012. Decay of ozone in water: a review. *Ozone Sci. Eng.* 34, 233–242.
- Goss, K.-U., 2008. The pK_a values of PFOA and other highly fluorinated carboxylic acids. *Environ. Sci. Technol.* 42, 456–458.
- Guan, Z., Guo, Y., Li, S., Feng, S., Deng, Y., Ou, X., et al., 2020. Decomplexation of heterogeneous catalytic ozonation assisted with heavy metal chelation for advanced treatment of coordination complexes of Ni. *Sci. Total Environ.* 732, 139223.
- Guan, Z., Guo, Y., Mo, Z., Chen, S., Liang, J., Liao, X., et al., 2022. High-efficiency treatment of electroless nickel plating effluent using core-shell MnFe₂O₄-C@Al₂O₃ combined with ozonation: performance and mechanism. *J. Hazard. Mater.* 433, 128768.
- Guo, J., Zhang, Y., Sun, Q., Qu, G., Wei, L., Wang, T., et al., 2022. Theoretical and experimental insights into electron-induced efficient defluorination of perfluorooctanoic acid and perfluorooctane sulfonate by mesoporous plasma. *Chem. Eng. J.* 430, 132922.
- He, J., Zheng, H., Ni, F., Shen, F., Xu, M., Tian, D., et al., 2023. Design and optimization of a novel Y-Fe-GO magnetic adsorbent for simultaneous removal of tetracycline and arsenic and adsorption mechanisms. *Chem. Eng. J.* 457, 141195.
- Huang, D., Yin, L., Niu, J., 2016. Photoinduced Hydrodefluorination mechanisms of Perfluorooctanoic acid by the SiC/graphene catalyst. *Environ. Sci. Technol.* 50, 5857–5863.
- Ji, B., Kang, P., Wei, T., Zhao, Y., 2020. Challenges of aqueous per- and polyfluoroalkyl substances (PFASs) and their foreseeable removal strategies. *Chemosphere* 250, 126316.
- Jothinathan, L., Cai, Q.Q., Ong, S.L., Hu, J.Y., 2022. Fe-Mn doped powdered activated carbon pellet as ozone catalyst for cost-effective phenolic wastewater treatment:

- mechanism studies and phenol by-products elimination. *J. Hazard. Mater.* 424, 127483.
- Khuntia, S., Majumder, S.K., Ghosh, P., 2015. Quantitative prediction of generation of hydroxyl radicals from ozone microbubbles. *Chem. Eng. Res. Des.* 98, 231–239.
- Kim, T.-H., Lee, S.-H., Kim, H.Y., Doudrick, K., Yu, S., Kim, S.D., 2019. Decomposition of perfluorooctane sulfonate (PFOS) using a hybrid process with electron beam and chemical oxidants. *Chem. Eng. J.* 361, 1363–1370.
- Kohantorabi, M., Moussavi, G., Oulego, P., Giannakis, S., 2022. Heterogeneous catalytic ozonation and peroxone-mediated removal of acetaminophen using natural and modified hematite-rich soil, as efficient and environmentally friendly catalysts. *Appl. Catal. B Environ.* 301, 120786.
- Kong, D., Zhao, Y., Fan, X., Wang, X., Li, J., Wang, X., et al., 2022. Reduced graphene oxide triggers Peracetic acid activation for robust removal of micropollutants: the role of Electron transfer. *Environ. Sci. Technol.* 56, 11707–11717.
- Kundu, S., Radian, A., 2022. Surface confinement of per-fluoroalkyl substances on an iron-decorated clay-cyclodextrin composite enables rapid oxidation by hydroxyl radicals. *Chem. Eng. J.* 431, 134187.
- Lai, C., Huang, F., Zeng, G., Huang, D., Qin, L., Cheng, M., et al., 2019. Fabrication of novel magnetic MnFe₂O₄/bio-char composite and heterogeneous photo-Fenton degradation of tetracycline in near neutral pH. *Chemosphere* 224, 910–921.
- Lai, L., Zhou, H., Zhang, H., Ao, Z., Pan, Z., Chen, Q., et al., 2020. Activation of peroxodisulfate by natural titanomagnetite for atrazine removal via free radicals and high-valent iron-oxo species. *Chem. Eng. J.* 387, 124165.
- Lee, Y.C., Li, Y.F., Chen, M.J., Chen, Y.C., Kuo, J., Lo, S.L., 2020. Efficient decomposition of perfluorooctanoic acid by persulfate with iron-modified activated carbon. *Water Res.* 174, 115618.
- Li, S., Li, X., Wu, H., Sun, X., Gu, F., Zhang, L., et al., 2019. Mechanism of synergistic effect on Electron transfer over Co–Ce/MCM-48 during ozonation of Pharmaceuticals in Water. *ACS Appl. Mater. Interfaces* 11, 23957–23971.
- Li, C., Wang, Y., Wang, Y., Wang, Z., Huang, Q., 2022a. Electrochemical oxidation combined with UV irradiation for synergistic removal of perfluorooctane sulfonate (PFOS) in water. *J. Hazard. Mater.* 436, 129091.
- Li, M., Jin, Y.-T., Yan, J.-F., Liu, Z., Feng, N.-X., Han, W., et al., 2022b. Exploration of perfluorooctane sulfonate degradation properties and mechanism via electron-transfer dominated radical process. *Water Res.* 215, 118259.
- Liang, J.-P., Zhou, X.-F., Zhao, Z.-L., Yang, D.-Z., Wang, W.-C., 2021. Degradation of trimethoprim in aqueous by persulfate activated with nanosecond pulsed gas-liquid discharge plasma. *J. Environ. Manag.* 278, 111539.
- Liang, X., Wang, X., Yang, M., Dong, H., Ji, Y., Wang, L., et al., 2023. α -Fe₂O₃-supported Co₃O₄ nanoparticles to construct highly active interfacial oxygen vacancies for ozone decomposition. *Environ. Pollut.* 330, 121704.
- Liu, C., Chang, V.W.C., Gin, K.Y.H., Nguyen, V.T., 2014. Genotoxicity of perfluorinated chemicals (PFCs) to the green mussel (*Perna viridis*). *Sci. Total Environ.* 487, 117–122.
- Liu, G., Li, C., Stewart, B.A., Liu, L., Zhang, M., Yang, M., et al., 2020. Enhanced thermal activation of peroxymonosulfate by activated carbon for efficient removal of perfluorooctanoic acid. *Chem. Eng. J.* 399, 125722.
- Logeshwaran, P., Sivaram, A.K., Surapaneni, A., Kannan, K., Naidu, R., Megharaj, M., 2021. Exposure to perfluorooctanesulfonate (PFOS) but not perfluorooctanoic acid (PFOA) at ppb concentration induces chronic toxicity in *Daphnia carinata*. *Sci. Total Environ.* 769, 144577.
- Lu, T., Chen, F., 2012. Multiwfn: a multifunctional wavefunction analyzer. *J. Comput. Chem.* 33, 580–592.
- Lu, T., Chen, Q., 2022. Realization of Conceptual Density Functional Theory and Information-Theoretic Approach in Multiwfn Program, 2. WILEY-VCH GmbH, pp. 631–647.
- Lyu, L., Zhang, L., Hu, C., 2016. Galvanic-like cells produced by negative charge nonuniformity of lattice oxygen on d-TiCuAl–SiO₂ nanospheres for enhancement of Fenton-catalytic efficiency. *Environ. Sci. Nano* 3, 1483–1492.
- Mahajan, J., Jeevanandam, P., 2018. Synthesis of TiO₂@ α -Fe₂O₃ core-shell heteronanostructures by thermal decomposition approach and their application towards sunlight-driven photodegradation of rhodamine B. *New J. Chem.* 42, 2616–2626.
- Mariussen, E., 2012. Neurotoxic effects of perfluoroalkylated compounds: mechanisms of action and environmental relevance. *Arch. Toxicol.* 86, 1349–1367.
- Niu, J., Lin, H., Gong, C., Sun, X., 2013. Theoretical and experimental insights into the electrochemical mineralization mechanism of Perfluorooctanoic acid. *Environ. Sci. Technol.* 47, 14341–14349.
- Ouyang, C., Wei, K., Huang, X., Gamal El-Din, M., Zhang, X., 2021. Bifunctional Fe for induced graphitization and catalytic ozonation based on a Fe/N-doped carbon–Al₂O₃ framework: theoretical calculations guided catalyst design and optimization. *Environ. Sci. Technol.* 55, 11236–11244.
- Ren, W., Xiong, L., Yuan, X., Yu, Z., Zhang, H., Duan, X., et al., 2019. Activation of Peroxydisulfate on carbon nanotubes: Electron-transfer mechanism. *Environ. Sci. Technol.* 53, 14595–14603.
- Saleh, H.M., Anuar, M.S.M., Simarani, K., 2017. Ultrasound degradation of xanthan polymer in aqueous solution: its scission mechanism and the effect of NaCl incorporation. *Ultrason. Sonochem.* 39, 250–261.
- Saravanan, A., Deivayanai, V.C., Kumar, P.S., Rangasamy, G., Hemavathy, R.V., Harshana, T., et al., 2022. A detailed review on advanced oxidation process in treatment of wastewater: mechanism, challenges and future outlook. *Chemosphere* 308, 136524.
- Shi, W., Liu, X., Liu, Y., Li, D., Tong, X., Ma, J., et al., 2023. Catalytic ozonation of hard COD in coking wastewater with Fe₂O₃/Al₂O₃-SiC: from catalyst design to industrial application. *J. Hazard. Mater.* 447, 130759.
- Singh, R.K., Fernando, S., Baygi, S.F., Multari, N., Thagard, S.M., Holsen, T.M., 2019. Breakdown products from Perfluorinated alkyl substances (PFAS) degradation in a plasma-based water treatment process. *Environ. Sci. Technol.* 53, 2731–2738.
- Song, Z., Zhang, Y., Liu, C., Xu, B., Qi, F., Yuan, D., et al., 2019. Insight into OH and O₂⁻ formation in heterogeneous catalytic ozonation by delocalized electrons and surface oxygen-containing functional groups in layered-structure nanocarbons. *Chem. Eng. J.* 357, 655–666.
- Song, G., Shi, G., Chen, L., Wang, X., Sun, J., Yu, L., et al., 2022. Different degradation mechanisms of low-concentration ozone for MIL-100(Fe) and MIL-100(Mn) over wide humidity fluctuation. *Chemosphere* 308, 136352.
- Sun, S., Sun, B., Zhu, X., Yang, Y., Liu, H., 2023. Defluorination of per-fluorinated compound (PFC) by microwave discharge plasma in liquid: a green and efficient water treatment technology. *Sep. Purif. Technol.* 319, 124071.
- Trojanowicz, M., Koc, M., 2013. Recent developments in methods for analysis of perfluorinated persistent pollutants. *Microchim. Acta* 180, 957–971.
- Vieira, V.M., Hoffman, K., Shin, H.-M., Weinberg, J.M., Webster, T.F., Fletcher, T., 2013. Perfluorooctanoic acid exposure and Cancer outcomes in a contaminated community: a geographic analysis. *Environ. Health Perspect.* 121, 318–323.
- Wang, J., Chen, H., 2020. Catalytic ozonation for water and wastewater treatment: recent advances and perspective. *Sci. Total Environ.* 704, 135249.
- Wang, Z., Jiang, J., Pang, S., Zhou, Y., Guan, C., Gao, Y., et al., 2018. Is sulfate radical really generated from Peroxydisulfate activated by Iron(II) for environmental decontamination? *Environ. Sci. Technol.* 52, 11276–11284.
- Wang, J., Shen, M., Gong, Q., Wang, X., Cai, J., Wang, S., et al., 2020. One-step preparation of ZVI-sludge derived biochar without external source of iron and its application on persulfate activation. *Sci. Total Environ.* 714, 136728.
- Wu, Z., Wang, X., Yao, J., Zhan, S., Li, H., Zhang, J., et al., 2021. Synthesis of polyethyleneimine modified CoFe₂O₄-loaded porous biochar for selective adsorption properties towards dyes and exploration of interaction mechanisms. *Sep. Purif. Technol.* 277, 119474.
- Xu, L., He, Z., Wei, X., Shang, Y., Shi, J., Jin, X., et al., 2023. Facile-prepared Fe/Mn coproduct biochar is an efficient catalyst for mediating the degradation of aqueous ibuprofen via catalytic ozonation. *Chem. Eng. J.* 461, 142028.
- Yang, J.S., Lai, W.W., Lin, A.Y., 2021. New insight into PFOS transformation pathways and the associated competitive inhibition with other perfluoroalkyl acids via photoelectrochemical processes using GOTO₂ film photoelectrodes. *Water Res.* 207, 117805.
- Yang, W., Ren, J., Li, J., Zhang, H., Ma, K., Wang, Q., et al., 2022. A novel Fe-co double-atom catalyst with high low-temperature activity and strong water-resistant for O₃ decomposition: a theoretical exploration. *J. Hazard. Mater.* 421, 126639.
- Yang, M., Du, Z., Bao, H., Zhang, X., Liu, Q., Guo, W., et al., 2023. Experimental and theoretical insight of Perfluorooctanoic acid destruction by alkaline hydrothermal treatment enhanced with zero-valent Iron in biochar. *ACS ES&T Water* 3, 1286–1293.
- Yu, D., Li, L., Wu, M., Crittenden, J.C., 2019a. Enhanced photocatalytic ozonation of organic pollutants using an iron-based metal-organic framework. *Appl. Catal. B Environ.* 251, 66–75.
- Yu, D., Wu, M., Hu, Q., Wang, L., Lv, C., Zhang, L., 2019b. Iron-based metal-organic frameworks as novel platforms for catalytic ozonation of organic pollutant: efficiency and mechanism. *J. Hazard. Mater.* 367, 456–464.
- Yu, G., Wang, Y., Cao, H., Zhao, H., Xie, Y., 2020. Reactive oxygen species and catalytic active sites in heterogeneous catalytic ozonation for water purification. *Environ. Sci. Technol.* 54, 5931–5946.
- Zhang, S., Wang, D., Quan, X., Zhou, L., Zhang, X., 2013. Multi-walled carbon nanotubes immobilized on zero-valent iron plates (Fe⁰-CNTs) for catalytic ozonation of methylene blue as model compound in a bubbling reactor. *Sep. Purif. Technol.* 116, 351–359.
- Zhang, Y., Lu, J., Yi, P., Zhang, Y., Wang, Q., 2019a. Trichloronitromethane formation from amino acids by preozonation-chlorination: the effects of ozone dosage, reaction time, pH, and nitrite. *Sep. Purif. Technol.* 209, 145–151.
- Zhang, Y., Moores, A., Liu, J., Ghoshal, S., 2019b. New insights into the degradation mechanism of Perfluorooctanoic acid by persulfate from density functional theory and experimental data. *Environ. Sci. Technol.* 53, 8672–8681.
- Zhang, J., Xin, B., Shan, C., Zhang, W., Dionysiou, D.D., Pan, B., 2021. Roles of oxygen-containing functional groups of O-doped g-C₃N₄ in catalytic ozonation: quantitative relationship and first-principles investigation. *Appl. Catal. B Environ.* 292, 120155.
- Zhou, Y., Lv, H., Lin, J., Lv, T., Wang, N., Tang, H., et al., 2022. Complete mechanochemical defluorination of perfluorooctanoic acid using Al₂O₃ and Al powders through matching electron-mediated reduction with decarboxylation. *Chemosphere* 307, 135872.
- Zoumpouli, G.A., Siqueira Souza, F., Petrie, B., F  ris, L.A., Kasprzyk-Hordern, B., Wenk, J., 2020. Simultaneous ozonation of 90 organic micropollutants including illicit drugs and their metabolites in different water matrices. *Environ. Sci.: Water Res. Technol.* 6, 2465–2478.